Environmental Science & Technology

pubs.acs.org/est

Article

Reducing Chloride Ion Permeation during Seawater Electrolysis Using Double-Polyamide Thin-Film Composite Membranes

Xuechen Zhou, Rachel F. Taylor, Le Shi, Chenghan Xie, Bin Bian, and Bruce E. Logan*

Cite This: *Environ. Sci. Technol.* 2024, 58, 391−399

Read Online

ACCESS | Metrics & More | Article Recommendations | Supporting Information

ABSTRACT: Low-cost polyamide thin-film composite membranes are being explored as alternatives to expensive cation exchange membranes for seawater electrolysis. However, transport of chloride from seawater to the anode chamber must be reduced to minimize the production of chlorine gas. A double-polyamide composite structure was created that reduced the level of chloride transport. Adding five polyamide layers on the back of a conventional polyamide composite membrane reduced the chloride ion transport by 53% and did not increase the applied voltage. Decreased chloride permeation was attributed to enhanced electrostatic and steric repulsion created by the new polyamide layers. Charge was balanced through increased sodium ion transport (52%) from the anolyte to the catholyte rather than through a change in the transport of protons and hydroxides. As a result, the Nernstian loss arising from the pH difference between the anolyte and catholyte remained relatively constant during electrolysis despite membrane modifications. This lack of a change in pH showed that transport of protons and hydroxides during electrolysis was independent of salt ion transport. Therefore, only sodium ion transport could compensate for the reduction of chloride flux to maintain the set current. Overall, these results prove the feasibility of using a double-polyamide structure to control chloride permeation during seawater electrolysis without sacrificing energy consumption.

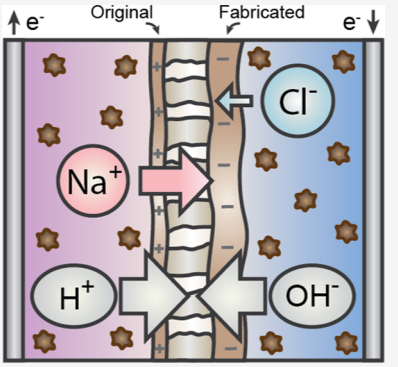

KEYWORDS: *seawater electrolysis, green hydrogen production, thin-film composite membrane, double-polyamide, chloride leakage, energy consumption*

INTRODUCTION

The global demand for hydrogen has been rising in recent years, with a 22% increase to 115 million tons per year expected by 2030.[1,2] Hydrogen gas is currently produced primarily via steam-methane reforming, which results in the generation of carbon monoxide and carbon dioxide.[3,4] Water electrolysis driven by renewable electricity (e.g., wind or solar power) for hydrogen production is a cleaner alternative.[5,6] However, ultrapure water is usually needed for water electrolysis, which is often not readily available in areas where renewable energy sources are abundant, like coastal regions, as salt water is prevalent in those regions.[7,8] Direct seawater electrolysis is problematic due to the evolution of corrosive chlorine gas at the anode, which can shorten the life span of the electrolyzer setup.[9,10] One potential solution is to pretreat seawater to produce ultrapure water for electrolysis, but this increases the complexity of hydrogen production.[11,12]

An asymmetric water electrolyzer configuration has recently been proposed that uses fully oxidized salts (e.g., sodium perchlorate) as contained anolyte and seawater as the catholyte to prevent chlorine evolution.[13] Low-cost (<$10 m^{-2})[13] polyamide (PA) thin-film composite (TFC) reverse osmosis membranes were used instead of more expensive cation exchange membranes ($250 to $500 m^{-2})[13] commonly used in acidic water electrolyzers to control the ion exchange between the catholyte and anolyte.[13,14] These PA TFC membranes exhibit high resistance to salt permeation due to steric exclusion.[15,16] Thus, applying TFC membranes to seawater electrolysis helps to limit the passage of chloride ions (Cl^-) into the anolyte and the leakage of the anolyte. Water ions, H^+ and OH^-, can easily transport through TFC membranes, which can decrease the membrane charge transfer resistance.[17,18]

One major concern is that the small amount of Cl^- ions passing through TFC membranes during seawater electrolysis still needs to be decreased to minimize chlorine generation.[13,19] Another concern is the energy loss due to the generation of a pH gradient when using TFC membranes and salty water. During electrolysis, H^+ ions are generated in the anode and OH^- ions are produced in the cathode. Although TFC membranes favor the transport of water ions over salt ions, some cross-membrane charge is still carried by salt ions, increasing the concentrations of H^+ in the anolyte and OH^- in

Received: September 3, 2023
Revised: December 5, 2023
Accepted: December 7, 2023
Published: December 26, 2023

the catholyte. This pH difference can contribute to the voltage increment during electrolysis, referred to as the Nernstian overpotential.[20,21] Using a membrane with a more selective PA active layer with negative charge was recently shown to moderately reduce the permeation of Cl^- ions but have little effect on the transport of counterions (Na^+) during electrolysis.[22] The Nernstian overpotential remained nearly constant and thus did not further decrease the energy demands. Therefore, other methods are needed to further reduce Cl^- ion transport in TFC membranes, ideally along with the deceleration of Na^+ ion permeation.

In this study, we examined the use of a double-polyamide TFC membrane structure for reducing the permeation of chloride ions during water electrolysis (Figure 1). It was

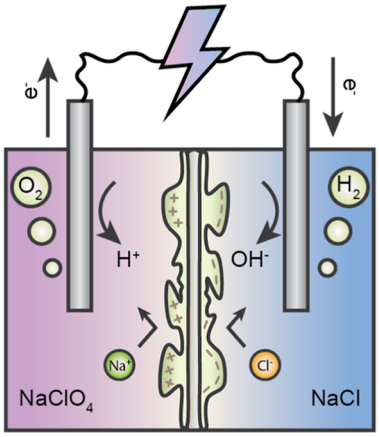

Figure 1. Schematic diagram showing the application of double-polyamide TFC membranes for seawater electrolysis. H^+ and oxygen gas are produced on the anode through water oxidation, and OH^- and hydrogen gas are produced on the cathode through water reduction. The transport of Na^+ ions is reduced by the positively charged polyamide layer facing the acidic anolyte, and the transport of Cl^- ions is reduced by the negatively charged polyamide layer facing the alkaline catholyte.

hypothesized that the negatively charged polyamide facing the alkaline catholyte would decrease the transport of negatively charged Cl^- ions into the anolyte, and the positively charged polyamide facing the acidic anolyte would reduce the transport of Na^+ ions into the catholyte. Hence, having a polyamide layer on both sides of the membrane would favor the transport of water ions due to their higher permeability in the PA layer. In addition, the rapid water ion transport can be maintained through very fast water ion association to form water molecules. To support the fabricated PA layer, an intermediate polydopamine (PDA) layer was added to the back side of the polysulfone (PSF) layer of a TFC membrane already containing a PA layer. The applied voltage needed to obtain a set current was used to monitor the impact of additional PA layers on energy use, and voltage variations were examined relative to possible changes in charge transfer resistance and Nernstian overpotential. Ion permeation during the electrolysis was analyzed by measuring the concentrations of salt ions in the electrolyte chambers.

MATERIALS AND METHODS

Materials and Chemicals. SW30 TFC reverse osmosis membranes (Dow Chemical; with fully aromatic PA) were used for all tests. Chemicals used were: sodium perchlorate ($NaClO_4$, anhydrous, 98.0−102.0%), potassium chloride (KCl, 99.0%), *m*-phenylenediamine (MPD, 99.0%), and 1,3,5-benzenetricarbonyl chloride (TMC, 98.0%) (Thermo Fisher Scientific); and sodium chloride (NaCl, 99.0%), dopamine hydrochloride, trizma hydrochloride (99.0%), and hexane (anhydrous, 95.0%) (Sigma-Aldrich). To ensure the purity of our solutions, we used deionized water (>18.2 MΩ·cm) produced by a Milli-Q ultrapure water purification system (Synergy).

Membrane Preparation. To add the second polyamide layer, TFC membranes were initially soaked in a solution of 25% isopropyl alcohol for 30 min to fully wet the membranes and remove any preservatives. After this, they were washed thoroughly with deionized (DI) water. The polyester (PET) fabric support layer was gently removed using tweezers, which can be done without affecting the properties of the active layer (Figure S1A).[23] After being attached to a glass plate using tape (Figure S1B), the back side of the remaining polymeric layers was exposed to 2 g L^{-1} dopamine solution (in 10 mM Tris buffer, pH 8.5) for 24 h to create a PDA intermediate layer.[24] The composite membrane (PDA side only) was then immersed in 3.3 wt % MPD water solution for 2 min, and the residual solution was removed using a rubber plate roller. The MPD-soaked composite membrane was then immersed in 0.15 wt % TMC in hexane for 1 min to form a thin PA film.[25] The newly fabricated PA layer was rinsed with hexane, air-dried for 2 min, rinsed with DI water, and stored in DI water at 4 °C for further use. To construct thicker PA layers (denoted as multiple PA layers), the composite membrane was repeatedly immersed in the MPD water solution and TMC in hexane until the desired thickness was achieved.

Material Characterization. X-ray photoelectron spectroscopy (XPS) experiments used a Physical Electronics VersaProbe III instrument equipped with a monochromatic Al Kα X-ray source ($h\nu$ = 1486.6 eV) and a concentric hemispherical analyzer. Charge neutralization was performed using both low-energy electrons (<5 eV) and argon ions. The binding energy axis was calibrated using sputter-cleaned Cu (Cu $2p_{3/2}$ = 932.62 eV, Cu $3p_{3/2}$ = 75.1 eV) and Au foils (Au $4f_{7/2}$ = 83.96 eV).[26] Peaks were charge-referenced to the CH_x band in the carbon 1s spectra at 284.8 eV. Measurements were made at a takeoff angle of 45° with respect to the sample surface plane. This resulted in a typical sampling depth of 3−6 nm (95% of the signal originated from this depth or shallower). Quantification was done using instrumental relative sensitivity factors (RSFs) that account for the X-ray cross-section and inelastic mean free path of the electrons. On homogeneous samples, major elements (>5 atom %) tend to have standard deviations of <3%, while minor elements can be significantly higher. The analysis size was ∼200 μm in diameter. Fourier transform infrared (FTIR) spectra were recorded in attenuated total reflection (ATR) geometry using a Bruker Vertex 80 instrument with an LN-MCT detector, equipped with Harrick Diamax ATR accessory using a germanium ATR crystal. IR spectra were recorded with 400 scans between 4000 and 500 cm^{-1} at a resolution of 6 cm^{-1}. Water contact angle measurements were performed with an automated dispensing system (Ramé-hart 260). During the measurement, a 10 μL drop of deionized water was used, and the captured image was analyzed using the DROPimage advance software. The morphology of the fabricated films was imaged with a field emission scanning electron microscope (SEM; Verios G4, Thermo-Scientific, OR).

https://doi.org/10.1021/acs.est.3c07248
Environ. Sci. Technol. 2024, 58, 391−399

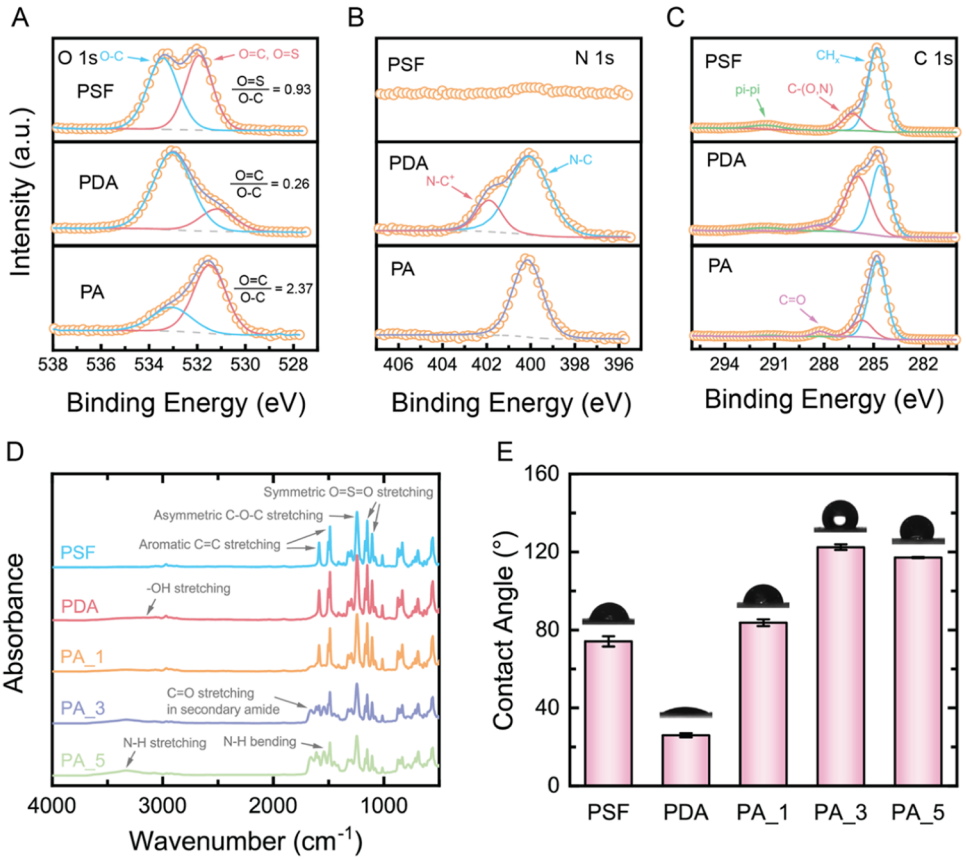

Figure 2. Characterization of the fabricated polymeric layers. (A) O 1s, (B) N 1s, and (C) C 1s XPS spectra of pristine PSF control, PDA coating layer, and the new PA active layer. (D) FTIR spectra and (E) water contact angle of pristine PSF control, PDA coating layer, and PA layers of varied thickness.

Seawater Electrolyzer Operation. A zero-gap flow cell (Scribner, North Carolina) was used to measure the applied voltage required to maintain a set current in the electrolyzer assembled with different membranes. Carbon cloth (2 × 2 cm^2) coated with 10% Pt/C catalyst was used for both electrodes for simplicity of electrode preparation (as opposed to more optimal or non-precious metal options), with the catalyst layers facing the membrane. The membranes (effective area of 4 cm^2) were set up between the two electrodes, with the original PA active layer facing the anode. To accurately measure salt ion crossover, $NaClO_4$ (1 M) was used in the anolyte as a nonreactive saline solution, and KCl (1 M) in the catholyte as synthetic seawater. KCl was used instead of NaCl in order to monitor the transport of cation from the catholyte into the anolyte. Both electrolytes (100 mL each) were recirculated at a flow rate of 25 mL min^{-1} with a peristaltic pump. Chronopotentiometry (CP) tests were conducted with a potentiostat (Biologic, VMP3) at a current density of 20 mA cm^{-2} for 6 h. For ion crossover tests, samples (1 mL) were taken from both the anolyte and catholyte at different time intervals. Ion chromatography (Dionex, Thermo Fisher Waltham, MA) was utilized to analyze the concentrations of Na^+ and ClO_4^- ions in the catholyte and K^+ and Cl^- ions in the anolyte. Electrochemical impedance spectroscopy (EIS) was conducted before and after electrolysis using an alternating current with a frequency range of 1 MHz to 100 mHz and a signal amplitude of 10 mV. The pH of both electrolytes was measured at the conclusion of the experiment.

RESULTS AND DISCUSSION

Material Characterization of the Constructed Polymeric Layers. XPS measurements confirmed the successful addition of the PDA and PA layers on the back side of the PSF layer, producing a membrane with PA layers on both sides. Before adding new polymeric layers, two oxygen peaks were observed within the XPS O 1s region of the PSF layer (Figure 2A). The peak with a binding energy of 531.9 eV was attributed to oxygen atoms bonded to sulfur with double bonds (O═S), while the peak with a binding energy of 533.4 eV was due to oxygen within the ether groups (O−C).[27] The atomic ratio of oxygen in O═S to oxygen in O−C was found to be 0.93, consistent with the 1:1 ratio of oxygen in O═S to oxygen in O−C in the PSF structure. After coating the PSF layer with PDA, the double-bonded oxygen atoms decreased to 26% of the single-bonded oxygen atoms.[28] This reduction is likely due to the abundance of hydroxyl groups within the PDA layer. With the addition of the PA layer, the amount of double-bonded oxygen atoms increased to 2.37 times the number of single-bonded oxygen atoms, which is contributed by the formation of amide groups.

No nitrogen was detected within the PSF layer, but nitrogen peaks appeared after coating the PSF layer with the additional PDA and PA layers (Figure 2B). Detailed deconvolution of the nitrogen peaks indicated that the nitrogen atoms mainly existed in the deprotonated form (N−C, binding energy of 400.1 eV)[29] within the PA layer, consistent with the limited unreacted amine groups within the PA layer. As a comparison, both protonated (N−C^+, binding energy of 401.9 eV)[29] and

https://doi.org/10.1021/acs.est.3c07248
Environ. Sci. Technol. 2024, 58, 391−399

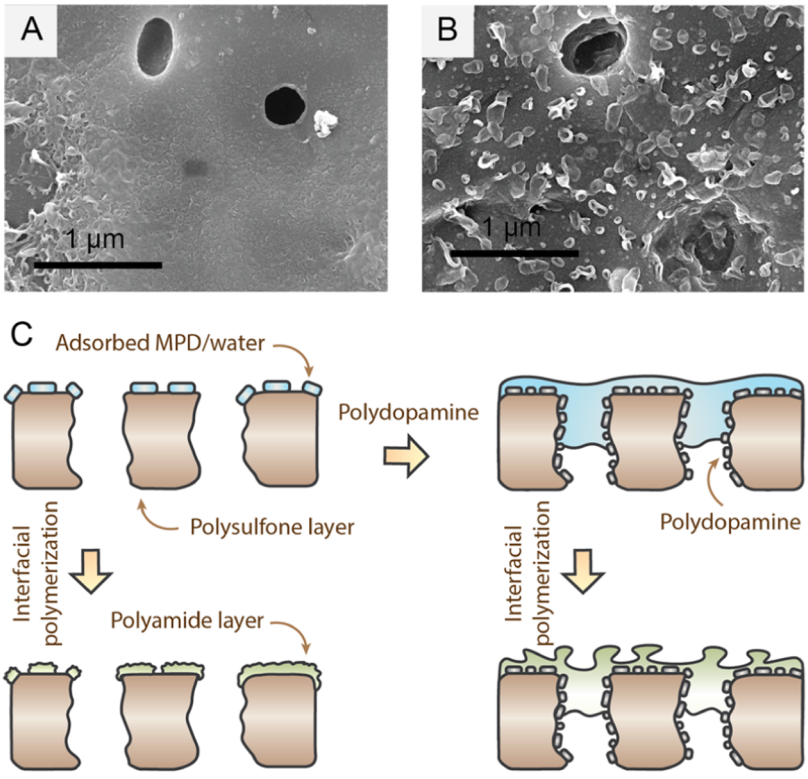

Figure 3. Rationalization for the polydopamine coating. SEM images of the (A) PA layer created directly on the PSF layer and (B) PA layer fabricated on the PDA-coated PSF layer. (C) Schematic diagram explaining the mechanism that the PDA layer enhanced the membrane wettability and narrowed the pore sizes of substrates, thus favoring the construction of pinhole-free PA layers with ridge-and-valley structure both on top of and inside the pores of the substrates.

deprotonated nitrogen (N−C) were observed within the PDA layer. The XPS C 1s region also supports the creation of PA layers, as carbonyl groups (binding energy of 288.1 eV) were observed within the PA C 1s region (Figure 2C).[29] These carbonyl groups were absent within the PSF and PDA C 1s region.

FTIR spectra confirmed the presence of new polymeric layers and variations in their thickness (Figure 2D). Peaks with wavenumbers of 1151 and 1106 cm^{-1} were attributable to symmetric O═S═O stretching within the PSF layer.[30] A peak with a wavenumber of 1246 cm^{-1} was due to asymmetric C−O−C stretching,[30] and peaks with the wavenumbers of 1584 and 1488 cm^{-1} were due to the aromatic C═C stretching within the benzene rings.[30] After the PDA coating, a new broad peak between wavenumbers of 2815 and 3666 cm^{-1} was observed within the FTIR spectrum, likely due to the appearance of hydroxyl groups within the PDA layer.[31] The creation of PA layers also resulted in new peaks in the FTIR spectrum. Peaks with the wavenumber of 1664 cm^{-1} were assigned to the C═O stretching within the secondary amide.[32] Additionally, the peak with the wavenumber of 1541 cm^{-1} was due to the N−H bending, and the peak between 3000 and 3684 cm^{-1} was attributed to N−H stretching.[33] The intensity of these peaks increased with the addition of new PA layers.

The constructed polymeric layers altered the hydrophilicity of the membrane surface (Figure 2E). The water contact angle of the PSF layer was reduced from 74 ± 3 to 26 ± 1° by coating it with a layer of PDA. This decrease can be attributed to the hydrophilic hydroxyl groups within the PDA layer covering the hydrophobic benzene rings in the PSF layer. Adding PA layers on top of the PDA layer increased the water contact angle to 117 ± 1° (5 polyamide layers) by covering the hydroxyl groups again with benzene rings within the PA layer.

Polydopamine Intermediate Layers. A PDA intermediate layer was needed to minimize the pinholes during the fabrication of the PA layers. When PA layers were added directly on top of the PSF layer, pinholes were observed on the fabricated layers (Figure 3A). With the inclusion of a PDA intermediate layer, these pinholes were filled with PA materials, resulting in the disappearance of the empty and dark regions (Figure 3B). A ridge-and-valley structure was also observed, which is characteristic of surfaces containing PA layers (Figure S2).[34] The improved formation of PA layers with the PDA intermediate layer was attributed to both the smaller pore size and the increased hydrophilicity of the substrate (Figure 3C). Constructing PA layers via interfacial polymerization involved wetting the substrate with an MPD aqueous solution and then reacting residual MPD molecules with TMC in hexane (Figure S1). When interfacial polymerization was carried out on the pristine PSF layer, only a few isolated aqueous droplets containing MPD were expected to remain on the substrate surface after the first step due to the hydrophobic nature of the PSF layer (Figure 2E). These droplets could not fill the large single-digit micrometer pores (Figure S3A). Consequently, when the substrate surface came into contact with the TMC solutions, defects remained within the fabricated PA layers. Coating the PSF substrate with the PDA layer not only narrowed the substrate pore size to submicrometer ranges (Figure S3B) but also increased the hydrophilicity of the surface (Figure 2E), facilitating the filling of the substrate pores with MPD solutions. As a result, pinholes within PA layers

https://doi.org/10.1021/acs.est.3c07248
Environ. Sci. Technol. 2024, 58, 391−399

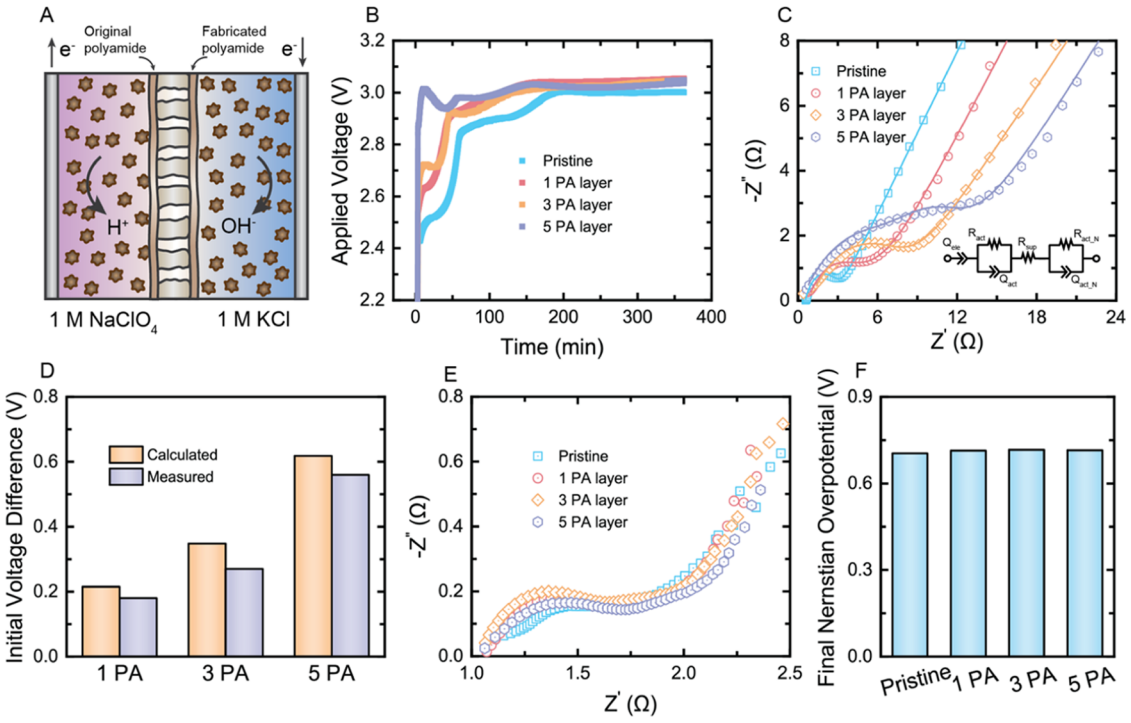

Figure 4. Operation of electrolyzers assembled with double-polyamide TFC membranes. (A) Schematic diagram of electrolyzers assembled with double-polyamide TFC membranes. (B) Applied voltage of electrolyzers assembled with double-polyamide TFC membranes with varied thickness. (C) EIS spectra of the electrolyzers at the beginning of the operation . (D) Initial voltage increases of the electrolyzers with the use of double-polyamide membranes. (E) EIS spectra of the electrolyzers at the end of the operation. (F) Nernstian overpotential of the electrolyzers at the end of the operation.

could be minimized by first forming a more suitable substrate for the addition of the PA material (Figure 3C).[35]

Applied Voltages for Seawater Electrolysis. When the pristine PA TFC membrane (i.e., original PA layer plus a PSF support layer) was utilized as the separator for the seawater electrolyzer (Figure 4A), the applied voltage to maintain a current of 20 mA cm^{-2} initially increased rapidly (to 2.45 V within 10 min) and then stabilized at 3.00 ± 0.00 V between 300 and 360 min (Figure 4B). With the addition of PA layers, the initial applied voltage increased more rapidly, with the initial increases of 2.63 V with one layer, 2.72 V with three layers, and 3.01 V with five layers. However, despite the significant enhancement in the initial applied voltage with the addition of PA layers, there was little difference observed between the applied voltage of these electrolyzers at the steady state with 3.05 ± 0.00 V with one PA layer, 3.04 ± 0.00 V with three layers, and 3.04 ± 0.01 V with five layers. Based on the average applied voltage, the overall increase in applied voltage by adding the PA layers was less than 2%.

EIS Analysis of Membrane Charge Transfer Resistance. Altering the separating membrane within the electrolyzer could impact the membrane charge transfer resistance and the Nernstian overpotential. Considering that the initial pH was 5.6 for all of the electrolytes, the significant surge in the applied voltage observed at the start of the operation was assumed to be due to an increase in the membrane charge transfer resistance. EIS spectroscopy was used to examine this hypothesis.

The comparison between the EIS spectra of the seawater electrolyzer systems during the initial period of each experiment showed that the addition of extra PA layers had little effect on the *x*-intercept but did increase the size of the semicircle in the EIS curves (Nyquist plot; Figure 4C). This difference in the EIS curves suggested that the PA layer could be analyzed as a parallel-connected capacitor and resistor (R_{act_N}) in the equivalent circuit of the electrolyzer system (Figure 4C).[36] Given the nonideality and leakage of "polyamide capacitors", constant phase elements (Q_{act_N}) are usually used for fitting instead of capacitors.[36] As a comparison, when we retained the original PA layer and modified the number of PET layers (i.e., the thickness of the support layer) on the back side of the membrane, we observed that the semicircle size of the EIS curves in the Nyquist plot was consistently maintained. However, the *x*-intercept showed an upward trend as the number of PET layers increased (Figure S4A). Based on this observation, we modeled the porous support layer of the composite membranes as a single resistor (R_{sup}) within the equivalent circuit of the overall system (Figure S4A).[36] To ensure a more precise calculation of the resistance of the newly fabricated PA layers (R_{act_N}), we first fitted the resistance of the original PA layer (R_{act}) using EIS curves obtained from TFC membranes with support layers of varied thicknesses (Figure S4A). The original PA layer resistance was then assumed to be a constant parameter, which we slightly optimized after fitting the EIS curves obtained from double-polyamide TFC membranes.

With the increase in PET layer thickness, the resistance of the support layer (R_{sup}) was increased from 2.2 Ω cm^2 (0 PET layer) to 12.8 Ω cm^2 (1 layer), 21.2 Ω cm^2 (2 layers), and 30.0 Ω cm^2 (3 layers) (Figure S4B). The resistance of the original PA layer (R_{act}) remained nearly consistent across all membranes, regardless of the number of PET layers present (Figure S4B), with an average of 10.9 ± 1.2 Ω cm^2. Fitting the EIS spectra collected with the electrolyzer systems assembled

https://doi.org/10.1021/acs.est.3c07248
Environ. Sci. Technol. 2024, 58, 391−399

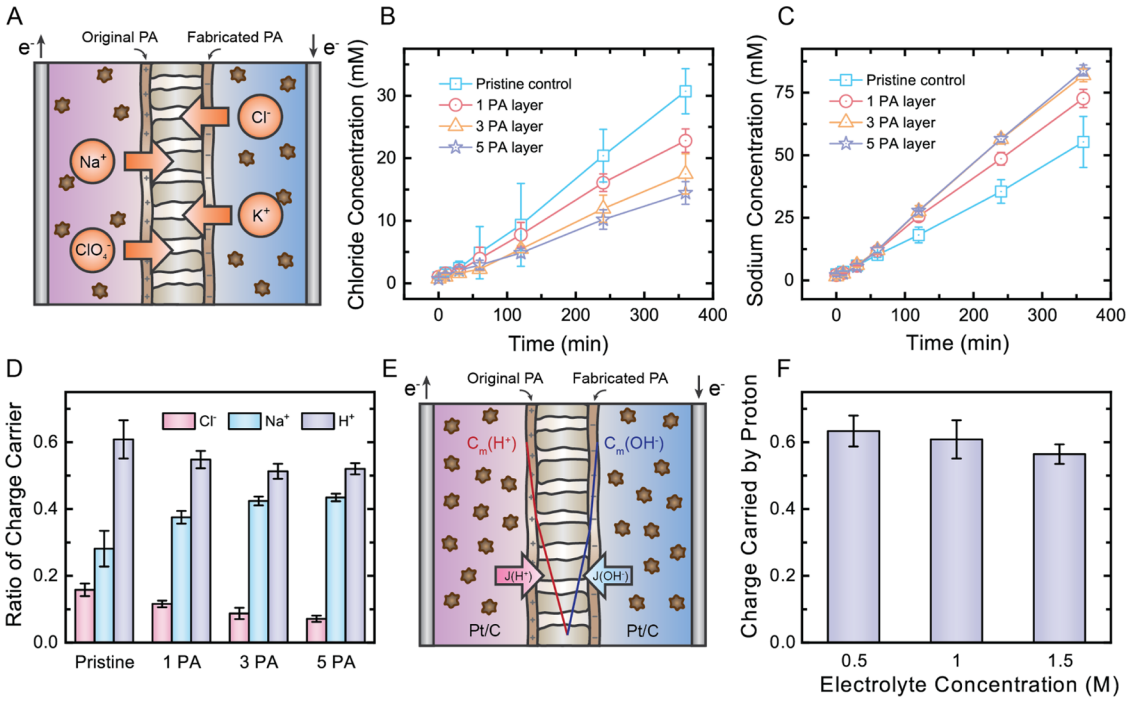

Figure 5. (A) Schematic diagram showing the direction of salt ion permeation within the electrolyzer. Increase of (B) chloride concentration in the anolyte and (C) sodium concentration in the catholyte over time within the electrolyzers assembled with double-polyamide TFC membranes with varied polyamide thicknesses (Text S1). (D) Ratio of charge carriers in each electrolyzer system. (E) Schematic diagram showing the transport of water ions within the flow cell. (F) Ratio of charge carried by proton through the pristine membrane at the electrolyte concentrations of 0.5, 1.0, and 1.5 M.

with double-polyamide membranes provides an average of 10.7 ± 0.7 Ω cm^2 for the original polyamide layers (R_{act}, Figure 4C), in line with the results obtained with the systems with membranes of varied PET layers. The resistances of the newly fabricated PA layers (R_{act_N}) were 10.8 Ω cm^2 (1 PA layer), 17.4 Ω cm^2 (3 PA layers), and 30.9 Ω cm^2 (5 PA layers), leading to higher voltage requirements of 0.22 V (1 PA layer), 0.35 V (3 PA layer), and 0.62 V (5 PA layers) at the set current of 20 mA cm^{-2} compared to the pristine membrane at the beginning of the electrolysis. These estimated initial voltage increases were slightly higher compared to the values directly measured (0.18 V for 1 PA layer, 0.27 V for 3 PA layers, 0.56 V for 5 PA layers; Figure 4D), likely due to the production of H^+ and OH^- ions lowering the difference between membrane charge transfer resistance. At the end of the operation, there was no noticeable difference between the EIS curves of the systems with the pristine membrane and the composite membranes with extra PA layers (Figure 4E), indicating that under steady-state conditions, all of the systems had similar membrane charge transfer resistances.

Independence of Nernstian Overpotential on Membrane Selectivity. After 6 h of electrolysis, there was a 12.0 pH difference between the anolyte and catholyte for the system with pristine membrane and a 12.1 pH difference for the systems with composite membranes with 1, 3, and 5 extra PA layers (Figure S5), leading to a Nernstian overpotential of ~0.71 V for all of the systems (Figure 4F). This constant Nernstian overpotential, along with the similar membrane charge transfer resistance (Figure 4E), corroborates the minimal effect of the additional PA layers on the applied voltage of the electrolyzer in the steady state. Therefore, using a double-polyamide TFC structure did not lower the Nernstian overpotential by promoting the transport of H^+ and OH^- ions.

Ion Permeation during Electrolysis. Ion transport through each separating membrane was measured to further understand the impact of the extra PA layers on the operation of the seawater electrolyzers (Figure 5A). Among the four salt ions, the permeation of Cl^- ions from the catholyte to the anolyte and Na^+ ions from the anolyte to the catholyte (Figure 5B,C) is more significant compared to the transport of K^+ and ClO_4^- ions (Figure S6). During electrolysis, the electric field drives cations (Na^+ and K^+ here) to the cathode and anions (Cl^- and ClO_4^- here) to the anode. Hence, the permeation of Cl^- and Na^+ ions is driven by both the electric field and the concentration gradient (Figure 5A). In contrast, the concentration gradient is the only driving force for the passage of K^+ and ClO_4^- ions, and the electric field helps to retain these ions in their respective electrolytes (Figure 5A). The faster transport of Cl^- and Na^+ ions suggests the dominance of the electric field in controlling ion permeation during electrolysis.

Cl^- ion permeation decreased as the number of PA layers increased (Figure 5B), consistent with our expectation based on the use of PA layers on both sides of the membrane. When the pristine membrane was used as the separator, the Cl^- concentration in the anolyte after 360 min of operation was 30.7 mM. With the addition of 1 extra PA layer, this value reduced by 26% to 22.8 mM, and with 3 extra layers, it decreased by 43% to 17.5 mM. With 5 extra PA layers added to the back side of the pristine membrane, the final Cl^- concentration in the anolyte was only 14.4 mM, an overall reduction of 53%. Thus, adding additional PA layers successfully reduced the permeation of Cl^- ions. This reduction in Cl^- ion transport into the anolyte was also observed when sodium salt (1 M NaCl) was used in the catholyte (Figure S7) rather than KCl, indicating the use of the potassium ion in the electrolyte was not a factor in chloride ion

https://doi.org/10.1021/acs.est.3c07248
Environ. Sci. Technol. 2024, 58, 391−399

transport. Likely, the enhanced resistance to Cl^- transport was due to a combination of steric resistance for ion transport through the fabricated dense PA layers and electrostatic repulsion by the negatively charged PA layers facing the alkaline catholyte (pH ∼ 13 according to Figure S5).

The addition of PA layers increased the permeation of Na^+ ions into the catholyte (Figure 5C), indicating that water ion transport did not compensate for the decrease in Cl^- ion transport. The final concentration of Na^+ ions in the catholyte was 55.3 mM with the pristine membrane as the separator. When the PA layers were added, there was a 31% increase in the Na^+ ion concentration to 72.7 mM (1 additional PA layer). Adding more PA layers further increased the Na^+ ion crossover to 81.9 mM (3 additional PA layers) and 83.9 mM (5 additional PA layers). The highly increased Cl^- exclusion in ion transport with 5 additional polyamide layers (i.e., 14.4 mM for Cl^- ions and 83.9 mM for Na^+ ions in the respective permeate electrolytes; Figure 5B,C) was due to the higher resistance for Cl^- permeation resulting from the fabricated thicker negatively charged polyamide layers compared to the resistance to Na^+ permeation due to the original single polyamide layer with positive charge.

At the end of the operation (360 min), the ratio of charge carried by Na^+ was enhanced from 0.28 with pristine membranes to 0.43 when using membranes with 5 additional PA layers as the separator (Figure 5D). The increase in the ratio of Na^+ transport surpassed the decline in the ratio of Cl^-, leading to a slight decline in the ratio of charge carried by water ions (cross-membrane transfer of both H^+ and OH^- ions followed by neutralization inside the membrane, simplified as charge carried by H^+ in Figure 5D). For example, the ratio of charge carried by water ions was 0.60 with pristine membranes, with a decline to 0.52 when using membranes with 5 additional PA layers as the separator (Figure 5D). This slight reduction in the transport of water ions is also consistent with the observed pH difference between the anolyte and catholyte, which was 12.0 with pristine membranes and 12.1 with double-polyamide composite membranes.

The enhanced Na^+ permeation with the addition of PA layers can be explained by the relative independence of the water ion transport from the salt ions such that only Na^+ ions can compensate for the reduced Cl^- transport to maintain the constant applied current. H^+ ions are generated through the oxidation of H_2O in the anode, and OH^- ions are produced in the cathode. The generated H^+ ions either cross the membranes to neutralize the OH^- ions ($J(H^+)$ and $J(OH^-)$ in Figure 5E) or permeate the reservoir. Given the large concentration gradients of H^+ and OH^- ions (Figure 5E), the transport of both the H^+ and OH^- inside the membrane should be mainly driven by these concentration gradients. Different from conventional membrane processes where ion concentrations at the membrane surface are greatly influenced by their bulk concentration, the H^+ and OH^- concentrations at the interface between the electrodes and the membrane ($C_m(H^+)$ and $C_m(OH^-)$ in Figure 5E) were primarily regulated by their generation rate. These concentrations remained almost constant at a constant applied current, leading to a steady driving force. Therefore, when extra PA layers were added to the back side of the pristine membranes, the overall resistance to cross-membrane water ion transport (especially to OH^- ions) increased, and thus both $J(H^+)$ and $J(OH^-)$ declined. As a result, the ratio of charge carried by the water ions decreased (Figure 5D). The added PA layers also reduced the Cl^- permeation. Therefore, to maintain the applied constant current, the Na^+ transport was enhanced.

The autonomy of the water ion transport from the salt ions was further supported by the resilience of the ratio of charge carried by water ions to the change in the electrolyte concentrations. Specifically, when we increased the concentration of both the anolyte and catholyte by 3 times (from 0.5 to 1.5 M), the final concentration of Na^+ in the catholyte only increased from 52.1 to 61.3 mM (Figure S8A) and the Cl^- concentration in the anolyte remained almost the same (25.4 for 0.5 M and 26.4 mM for 1.5 M, Figure S8B). This insignificant change in the salt passage thus leads to a marginal alternation in the proportion of charge carried by water ions (0.63 for 0.5 and 0.56 for 1.5 M, Figure 5F). This lack of a change in water ion transport implies the fraction of charge carried by water ions is dictated by their rate of generation at the electrodes and their concentration gradient in the membrane, rather than their relative abundance in the solution.

Implications. In this study, composite membranes featuring double PA layers were constructed for seawater electrolysis applications. Our findings indicated that Cl^- ion permeation was considerably reduced during seawater electrolyzer operation due to enhanced steric and electrostatic repulsion of these ions with the membrane. Despite doubling the size-selective PA active layers and adding resistance to the Na^+ transport, the reduced Cl^- transport was mainly compensated for by the enhanced permeation of Na^+ ions into the catholyte, resulting in a nearly constant Nernstian overpotential. The lack of change in this overpotential was attributed to the independence of water ion transport from salt ion transport. To further explore this concept of using two active layers, future studies could examine the design of double-polyamide membranes with differently charge-modified PA layers (e.g., the layer facing the anode is highly positively charged and the layer facing the cathode is highly negatively charged) and their impact on the Cl^- ion permeation and energy consumption during seawater electrolysis.

■ ASSOCIATED CONTENT

Supporting Information

The Supporting Information is available free of charge at https://pubs.acs.org/doi/10.1021/acs.est.3c07248.

Double-polyamide TFC membrane preparation (Figure S1); SEM images of the original PA layer (Figure S2); SEM images of the pristine PSF and the PDA-coated PSF layer (Figure S3); EIS spectra of the electrolyzers assembled with TFC membranes with different PET thickness and the fitted resistances of the active layers and support layers (Figure S4); pH of the electrolytes at the end of electrolysis (Figure S5); perchlorate and potassium permeation, and proton accumulation within the electrolyzers (Figure S6); anion permeation when using sodium salts as the catholyte (Figure S7), and sodium and chloride ion permeation when varying the electrolyte concentrations (Figure S8) (PDF)

■ AUTHOR INFORMATION

Corresponding Author

Bruce E. Logan − *Department of Civil and Environmental Engineering, The Pennsylvania State University, University Park, Pennsylvania 16802, United States; Department of Chemical Engineering, The Pennsylvania State University,*

https://doi.org/10.1021/acs.est.3c07248
Environ. Sci. Technol. 2024, 58, 391−399

University Park, Pennsylvania 16802, United States; orcid.org/0000-0001-7478-8070; Phone: +1 (814) 8637908; Email: blogan@psu.edu

Authors

Xuechen Zhou − *Department of Civil and Environmental Engineering, The Pennsylvania State University, University Park, Pennsylvania 16802, United States;* orcid.org/0000-0001-8007-4787

Rachel F. Taylor − *Department of Chemical Engineering, The Pennsylvania State University, University Park, Pennsylvania 16802, United States;* orcid.org/0000-0002-2576-8193

Le Shi − *Department of Civil and Environmental Engineering, The Pennsylvania State University, University Park, Pennsylvania 16802, United States; College of Environmental and Resource Sciences, Zhejiang University, Hangzhou 310058, P. R. China;* orcid.org/0000-0003-1794-1256

Chenghan Xie − *Department of Civil and Environmental Engineering, The Pennsylvania State University, University Park, Pennsylvania 16802, United States;* orcid.org/0000-0002-4962-9737

Bin Bian − *Department of Civil and Environmental Engineering, The Pennsylvania State University, University Park, Pennsylvania 16802, United States;* orcid.org/0000-0001-5270-4964

Complete contact information is available at: https://pubs.acs.org/10.1021/acs.est.3c07248

Notes

The authors declare no competing financial interest.

■ ACKNOWLEDGMENTS

This research was funded by National Science Foundation grant CBET-2027552 and Penn State University through the Stan and Flora Kappe endowment.

■ REFERENCES

(1) *Global Hydrogen Review 2022*; International Energy Agency: Paris, 2022; p 5.

(2) Ball, M.; Wietschel, M. The future of hydrogen - opportunities and challenges. *Int. J. Hydrogen Energy* **2009**, *34* (2), 615−627.

(3) *Hydrogen Strategy: Enabling a Low-Carbon Economy*; United States Department of Energy: Washinton, DC, 2020.

(4) LeValley, T. L.; Richard, A. R.; Fan, M. H. Development of catalysts for hydrogen production through the integration of steam reforming of methane and high temperature water gas shift. *Energy* **2015**, *90*, 748−758.

(5) Lee, H.; Lee, B.; Byun, M.; Lim, H. Economic and environmental analysis for PEM water electrolysis based on replacement moment and renewable electricity resources. *Energy Convers. Manage.* **2020**, *224*, No. 113477.

(6) Chi, J.; Yu, H. M. Water electrolysis based on renewable energy for hydrogen production. *Chin. J. Catal.* **2018**, *39* (3), 390−394.

(7) Farràs, P.; Strasser, P.; Cowan, A. J. Water electrolysis: Direct from the sea or not to be? *Joule* **2021**, *5* (8), 1921−1923.

(8) Gao, F. Y.; Yu, P. C.; Gao, M. R. Seawater electrolysis technologies for green hydrogen production: challenges and opportunities. *Curr. Opin. Chem. Eng.* **2022**, *36*, No. 100827.

(9) Tong, W. M.; Forster, M.; Dionigi, F.; Dresp, S.; Erami, R. S.; Strasser, P.; Cowan, A. J.; Farras, P. Electrolysis of low-grade and saline surface water. *Nat. Energy* **2020**, *5* (5), 367−377.

(10) Zheng, W. R.; Lee, L. Y. S.; Wong, K. Y. Improving the performance stability of direct seawater electrolysis: from catalyst design to electrode engineering. *Nanoscale* **2021**, *13* (36), 15177−15187.

(11) Abba, S. I.; Benaafi, M.; Aljundi, I. H. Intelligent process optimization based on cutting-edge emotional learning for performance evaluation of NF/RO of seawater desalination plant. *Desalination* **2023**, *550*, No. 116376.

(12) Ludwig, H. Hybrid systems in seawater desalination - practical design aspects, present status and development perspectives. *Desalination* **2004**, *164* (1), 1−18.

(13) Shi, L.; Rossi, R.; Son, M.; Hall, D. M.; Hickner, M. A.; Gorski, C. A.; Logan, B. E. Using reverse osmosis membranes to control ion transport during water electrolysis. *Energy Environ. Sci.* **2020**, *13* (9), 3138−3148.

(14) Taylor, R.; Shi, L.; Zhou, X. C.; Rossi, R.; Picioreanu, C.; Logan, B. E. Electrochemical and hydraulic analysis of thin-film composite and cellulose triacetate membranes for seawater electrolysis applications. *J. Membr. Sci.* **2023**, *679*, No. 121692.

(15) Zhou, X. C.; Zhao, Y. Y.; Kim, S. R.; Elimelech, M.; Hu, S.; Kim, J. H. Controlled TiO2 growth on reverse osmosis and nanofiltration membranes by atomic layer deposition: Mechanisms and potential applications. *Environ. Sci. Technol.* **2018**, *52* (24), 14311−14320.

(16) Guan, Y. F.; Boo, C.; Lu, X. L.; Zhou, X. C.; Yu, H. Q.; Elimelech, M. Surface functionalization of reverse osmosis membranes with sulfonic groups for simultaneous mitigation of silica scaling and organic fouling. *Water Res.* **2020**, *185*, No. 116203.

(17) Stolov, M.; Freger, V. Ion transport and specificity in polyamide membranes studied by conductivity and its activation energy. *J. Membr. Sci.* **2023**, *678*, No. 121616.

(18) Kezia, K.; Lee, J.; Ogieglo, W.; Hill, A.; Benes, N. E.; Kentish, S. E. The transport of hydronium and hydroxide ions through reverse osmosis membranes. *J. Membr. Sci.* **2014**, *459*, 197−206.

(19) Logan, B. E.; Shi, L.; Rossi, R. Enabling the use of seawater for hydrogen gas production in water electrolyzers. *Joule* **2021**, *5* (4), 760−762.

(20) Rossi, R.; Hall, D. M.; Shi, L.; Cross, N. R.; Gorski, C. A.; Hickner, M. A.; Logan, B. E. Using a vapor-fed anode and saline catholyte to manage ion transport in a proton exchange membrane electrolyzer. *Energy Environ. Sci.* **2021**, *14* (11), 6041−6049.

(21) Rossi, R.; Taylor, R.; Logan, B. E. Increasing the electrolyte salinity to improve the performance of anion exchange membrane water electrolyzers. *ACS Sustainable Chem. Eng.* **2023**, *11*, 8573−8579, DOI: 10.1021/acssuschemeng.3c01245.

(22) Zhou, X. C.; Shi, L.; Taylor, R. F.; Xie, C. H.; Bian, B.; Picioreanu, C.; Logan, B. E. Relative insignificance of polyamide layer selectivity for seawater electrolysis applications. *Environ. Sci. Technol.* **2023**, *57* (39), 14569−14578.

(23) Wang, J. B.; Kingsbury, R. S.; Perry, L. A.; Coronell, O. Partitioning of alkali metal salts and boric acid from aqueous phase into the polyamide active layers of reverse osmosis membranes. *Environ. Sci. Technol.* **2017**, *51* (4), 2295−2303.

(24) Cheng, W.; Lu, X. L.; Kaneda, M.; Zhang, W.; Bernstein, R.; Ma, J.; Elimelech, M. Graphene oxide-functionalized membranes: The importance of nanosheet surface exposure for biofouling resistance. *Environ. Sci. Technol.* **2020**, *54* (1), 517−526.

(25) Lu, X. L.; Elimelech, M. Fabrication of desalination membranes by interfacial polymerization: history, current efforts, and future directions. *Chem. Soc. Rev.* **2021**, *50* (11), 6290−6307.

(26) Seah, M. P. Summary of ISO/TC 201 Standard: VII ISO 15472:2001 - surface chemical analysis - x-ray photoelectron spectrometers - calibration of energy scales. *Surf. Interface Anal.* **2001**, *31* (8), 721−723.

(27) Sánchez, S.; Pumera, M.; Fabregas, E.; Bartroli, J.; Esplandiu, M. J. Carbon nanotube/polysulfone soft composites: preparation, characterization and application for electrochemical sensing of biomarkers. *Phys. Chem. Chem. Phys.* **2009**, *11* (35), 7721−7728.

(28) Liu, Y. C.; Jiang, H. T.; Liu, C. M.; Ge, Y. L.; Wang, L.; Zhang, B.; He, H.; Liu, S. J. Influence of functional groups on toxicity of carbon nanomaterials. *Atmos. Chem. Phys.* **2019**, *19* (12), 8175−8187.

(29) Kaneda, M.; Lu, X. L.; Cheng, W.; Zhou, X. C.; Bernstein, R.; Zhang, W.; Kimura, K.; Elimelech, M. Photografting graphene oxide

to inert membrane materials to impart antibacterial activity. *Environ. Sci. Technol. Lett.* **2019**, *6* (3), 141−147.
(30) Singh, S.; Varghese, A. M.; Reddy, K. S. K.; Romanos, G. E.; Karanikolos, G. N. Polysulfone mixed-matrix membranes comprising poly(ethylene glycol)-grafted carbon nanotubes: mechanical properties and CO2 separation performance. *Ind. Eng. Chem. Res.* **2021**, *60* (30), 11289−11308.
(31) Zangmeister, R. A.; Morris, T. A.; Tarlov, M. J. Characterization of polydopamine thin films deposited at short times by autoxidation of dopamine. *Langmuir* **2013**, *29* (27), 8619−8628.
(32) Ghaemy, M.; Barghamadi, M. Synthesis and characterization of novel photoactive polyamide derived from substituted fluorene by Copper (I) catalyst. *J. Appl. Polym. Sci.* **2009**, *114* (6), 3464−3471.
(33) Porubská, M.; Szollos, O.; Konova, A.; Janigova, I.; Jaskova, M.; Jomova, K.; Chodak, I. FTIR spectroscopy study of polyamide-6 irradiated by electron and proton beams. *Polym. Degrad. Stab.* **2012**, *97* (4), 523−531.
(34) Elimelech, M.; Phillip, W. A. The future of seawater desalination: Energy, technology, and the environment. *Science* **2011**, *333* (6043), 712−717.
(35) Dai, R. B.; Han, H. Y.; Wang, T. L.; Li, J. Y.; Wu, Z. C.; Tang, C. Y. Y.; Wang, Z. W. Cleaning-healing-interfacial polymerization strategy for upcycling real end-of-life polyvinylidene fluoride microfiltration membranes. *ACS Sustainable Chem. Eng.* **2021**, *9* (30), 10352−10360.
(36) Shaffer, D. L.; Feldman, K. E.; Chan, E. P.; Stafford, G. R.; Stafford, C. M. Characterizing salt permeability in polyamide desalination membranes using electrochemical impedance spectroscopy. *J. Membr. Sci.* **2019**, *583*, 248−257.

https://doi.org/10.1021/acs.est.3c07248
Environ. Sci. Technol. 2024, 58, 391−399